

# The effect of stellar rotation on black hole mass and spin

Sohan Ghodla<sup>★1</sup>, J. J. Eldridge<sup>1</sup>

<sup>1</sup>*Department of Physics, University of Auckland, Private Bag 92019, Auckland, New Zealand*

Accepted XXX. Received YYY; in original form ZZZ

## ABSTRACT

The gravitational wave signature of a binary black hole (BBH) merger is dependent on its component mass and spin. If such black holes originate from rapidly rotating progenitors, the large angular momentum reserve in the star could drive a collapsar-like supernova explosion, hence substantially impacting these characteristics of the black holes in the binary. To examine the effect of stellar rotation on the resulting black hole mass and spin, we conduct a 1D general relativistic study of the end phase of the collapse. We find that the resulting black hole mass at times differ significantly from the previously assumed values. We quantify the dependence of the black hole spin magnitude on the hydrodynamics of the accretion flow, providing analytical relations for calculating the mass and spin based on the progenitor’s pre-collapse properties. Depending on the nature of the accretion flow, our findings have implications for the black hole upper mass gap resulting from pair-instability supernovae, the maximum mass of a maximally rotating stellar black hole ( $M_{\text{BH,max}} \approx 35M_{\odot}$ ), and the maximum effective spin of a BBH formed in tidally locked helium star - black hole binary ( $\chi_{\text{eff,max}} \approx 0.325$ ).

**Key words:** accretion disks – gravitational waves – black hole physics – gamma-ray burst: general

## 1 INTRODUCTION

The black hole masses resulting from rapidly rotating pre-collapse stars are not well described by the pre-existing prescriptions that estimate the remnant mass produced at core-collapse (e.g. Fryer & Kalogera 2001; Eldridge & Tout 2004; Fryer et al. 2012). The most widely used remnant mass functions (resulting from the supernova explosion) are based on the work of Fryer et al. (2012). They offer two variations of supernova models to calculate the resulting compact remnant mass, namely the *Delayed* and *Rapid* explosion mechanisms. Both models rely on convection-enhanced neutrino heating (Herant et al. 1994; see Fryer et al. 2021 for a recent review) to drive a successful explosion. The primary difference between them lies in the instability that could drive such an explosion. The Delayed mechanism is driven by a standing accretion shock instability (Blondin et al. 2003) and can produce an explosion with a delay of up to 1s after the bounce, while the Rapid mechanism utilizes the Rayleigh-Taylor instability (e.g., Sharp 1984), and the explosion occurs within 0.25s. Under a failed explosion, the Rapid mechanism leads to a direct collapse, while in the Delayed mechanism, some form of explosion may still be possible.

On the other hand, for progenitor stars with a substantial reservoir of angular momentum at core collapse, the supernova explosion might not be determined by convection and therefore may lead to remnant masses different from those predicted by the convection paradigm. This is because the angular momentum reservoir acts as an additional means of centrifugal support and the subsequent vis-

cous dynamics offer an efficient mechanism for energy dissipation during the episode of the explosion.

Fryer et al. (2012) assumed that under the scenario of substantial rotation, the occurrence of relativistic jets during core collapse (e.g., Woosley 1993; MacFadyen & Woosley 1999) would likely disrupt most of the star and only  $\approx 5M_{\odot}$  black hole would be produced. However, a number of subsequent studies, although at times working in the paradigm of rapidly rotating progenitor stars, have either continued to use the Fryer et al. (2012) remnant mass function (e.g., Bavera et al. 2020; Riley et al. 2021) or assumed a more or less direct collapse - i.e., a major mass fraction of the pre-core collapse star ending up in the black hole, with some (typically the envelope) mass lost during the explosion (e.g., Mandel & de Mink 2016; Marchant et al. 2016; Qin et al. 2018; du Buisson et al. 2020). This is primarily due to the lack of a mass function that captures the effect of stellar rotation on the resulting black hole masses.

Another property of astrophysical black holes is their spin angular momentum, which, together with their mass, fully determines their property (Israel 1967; Carter 1971; Bekenstein 1972). Although 1D studies exist that take into account the spin evolution of the black hole during collapse of the star (e.g., Batta & Ramirez-Ruiz 2019; Bavera et al. 2020; Fuller & Lu 2022), they either do not account for the effect of wind outflows (e.g., Bavera et al. 2020, a strong magnetic field and/or relativistic dynamics on the nature of the accretion flow (Batta & Ramirez-Ruiz 2019; Bavera et al. 2020; Fuller & Lu 2022)). In this paper, we aim to address these shortcomings.

The collapse of a sufficiently rapidly rotating star should happen via the formation of an equatorial accretion disk. Such a supernova explosion paradigm, consisting of a newly formed spinning

★ sgho069@aucklanduni.ac.nz

black hole penetrated by a strong magnetic field of the surrounding accretion disk, is also known as a collapsar (Woosley 1993; MacFadyen & Woosley 1999) and is believed to be primarily responsible for the observed long-duration  $\gamma$ -ray bursts (GRBs). The dynamics of the accretion flow under a collapsar scenario has been extensively studied in the past (e.g., Gammie et al. 2004; Lee & Ramirez-Ruiz 2006; Kumar et al. 2008; Tchekhovskoy et al. 2010, 2011; Sądowski et al. 2014; Sądowski & Narayan 2016; Fujibayashi et al. 2020; Fujibayashi et al. 2023; Murguia-Berthier et al. 2020; Gottlieb et al. 2023; Jacquemin-Ide et al. 2023). The disk evolves viscously via magnetohydrodynamics, resulting in mass outflow and a transient energetic electromagnetic outburst. The resulting dynamics could be highly non-linear, and a detailed study would require a full 3-dimensions magneto-hydrodynamic simulation (e.g., Sądowski & Narayan 2016). However, conducting such simulations is computationally expensive and time-consuming.

For the current work, we use a simpler approach based on the earlier work of Kumar et al. (2008) - and later numerically implemented in Fuller & Lu (2022), which is a 1D non-relativistic, height-integrated, time-averaged formalism, but takes into account the effect of vertical wind outflows. We extend their work to a general relativistic framework, hence allowing us to more accurately consider the influence on the accretion flow in the inner region of the accretion disk around the proto-Kerr black hole. Since our calculations are time-averaged, most of the non-linearity would be averaged out. We adopt two variable approaches for treating the accretion flow in the near-horizon region, namely the Novikov & Thorne (1973) accretion disk formalism and the magnetically arrested accretion disk (Tchekhovskoy et al. 2011) formalism. We use this framework in conjunction with the MESA generated stellar models to calculate the resulting black hole mass and spin relations that would be suitable for black holes born from rotating stars. We then compare our results with the earlier work of Fryer et al. (2012), showcasing the crucial difference between the two. We also discuss some implications of our work for the expected birth properties of stellar black holes.

The remainder of this paper is organized as follows. In Section 2, we discuss details of the MESA models used in our analysis. Here, we also develop the formalism used for treating the collapsar dynamics. In Section 3, we present the mass and spin functions for black holes born from rotating stars and discuss their domain of validity. Then, in Section 4, we present some implications of our results, followed by a brief conclusion in Section 5.

## 2 METHOD

### 2.1 Models for rotating stars

We use MESA (Paxton et al. 2011, 2013, 2015, 2018, 2019) to evolve models of variably rotating single stars in the mass range  $5-95 M_{\odot}$  from the onset of helium burning to the core carbon depletion<sup>1</sup>. No substantial change in the relevant structure (or the angular momentum reservoir) of the star is expected past core carbon depletion, as is evident from the output of such evolved MESA models (e.g., see Fuller & Lu 2022).

Our stellar models exhibit a uniform initial rotation profile at various angular velocities. In MESA, rotation is treated in a shellular approximation (Zahn 1992; Meynet & Maeder 1997), implying that isobaric shells have uniform angular velocity. As the models evolve,

they lose mass and hence angular momentum. In addition, the angular momentum is redistributed internally, causing the rotation profile to deviate from that of the initial solid body. In MESA, the transfer of angular momentum is modeled in a diffusive approximation. This is accomplished by contribution from ordinary diffusion, meridional circulations (e.g., Eddington 1925; Sweet 1950), and the magnetic field instability-induced Spruit-Taylor dynamo (Spruit 2002). Although the mapping between the initial and final angular velocities is nonlinear, we choose a sufficient number of models (900+) such that it results in stars with different levels of final angular momentum reserves.

We use the Dutch wind mass loss scheme with the `Dutch_scaling_factor` = 0.25 and consider only a single metallicity with  $Z = 10^{-4}$ . Since the results in Section 3 are calculated so that they remain only a function of the final mass and the angular momentum of the collapsing star, the metallicity of the star is not the variable of interest. However, metallicity would play a direct role in determining the amount of mass and angular momentum that is retained by the star. For certain exceptional cases (e.g., those where angular momentum is sourced from the tidal influence of a binary companion), the angular momentum content can remain large even at larger metallicity; therefore, our approach remains valid for such cases as well.

### 2.2 Formalism for collapsar dynamics

Our goal is to determine the final mass and spin of the black hole resulting from the collapse of a rotating star of a given mass and angular momentum distribution. For such a purpose, the detailed nature of the collapse and the dynamics of the evolution of the accretion disk might not be necessary. As such, we focus on the effective (i.e. time-averaged) dynamics of the accretion flow, as detailed below. Unless explicitly stated, we use geometric units with  $G, c = 1$  throughout this section.

#### 2.2.1 Background geometry

As an initial condition, we assume that a natal black hole of some mass promptly forms during the initial collapse of the stellar core. The spacetime of this black hole (i.e., ignoring the remaining matter) can be modeled using the Kerr metric ( $g_{ab}$ ) whose line element in the Boyer-Lindquist coordinates ( $x^a := t, r, \theta, \phi$ ) reads

$$ds^2 = g_{ab} dx^a dx^b = - \left( 1 - \frac{2Mr}{\rho^2} \right) dt^2 - \frac{4Mar \sin^2 \theta}{\rho^2} d\phi dt + \frac{\rho^2}{\Delta} dr^2 + \rho^2 d\theta^2 + \left( r^2 + a^2 + \frac{2Mr a^2 \sin^2 \theta}{\rho^2} \right) \sin^2 \theta d\phi^2, \quad (1)$$

where  $a = J/M$ ;  $\Delta = r^2 - 2Mr + a^2$  and  $\rho^2 = r^2 + a^2 \cos^2 \theta$ . Here,  $M, J$  are the black hole's ADM mass and angular momentum, respectively. As the remainder of the stellar matter falls inwards, the metric evolves due to a change in the black hole mass and spin.

For simplicity, we assume that at any given time there is a negligible amount of matter in the equatorial plane such that the effect of the disk mass on the form of Eq. 1 can be ignored. Additionally, we assume that the outer shells have a nearly spherical configuration such that the spacetime inside the innermost infalling shell can be assumed to be flat (except for the effect due to the black hole). There are two Killing vector fields ( $\xi, \eta$ ) associated with this stationary, axisymmetric spacetime namely  $\xi = (1, 0, 0, 0) \partial_t$  and  $\eta = (0, 0, 0, 1) \partial_\phi$ . They correspond to the conservation of energy and the axial component of the angular momentum, respectively.

<sup>1</sup> The inlists for the MESA model, and the PYTHON script consisting of the numerical implementation of the formalism discussed in Section 2.2 can be found in the data availability statement.

### 2.2.2 The rotating fluid

The final states of a massive star evolved through MESA constitute the initial state of the following analysis. Prior to collapse, we assume (in accordance with the MESA model) that the stellar fluid comprises of matter, with only the axial component of angular momentum being nonzero. Let  $u^a$  be the 4-velocity of a fluid element of this star with components  $(u^t, u^r, u^\theta, u^\phi)$  in Boyer-Lindquist coordinates<sup>2</sup>. When the core experiences a collapse, the outer shells will initially be in a free fall. During this phase, we model stellar matter as a perfect fluid with the stress-energy tensor.

$$T^{ab} = (\rho + \epsilon + P)u^a u^b + P g^{ab}, \quad (2)$$

where  $g^{ab}$  is the “inverse” metric,  $P$  is the pressure and  $\rho, \epsilon$  are the rest mass and internal energy density. We further assume that  $\rho \gg (\epsilon + P)$ . This reduces Eq. 2 to a dust equation of state. Since the pressure approaches the energy density only in the inner region of the disk, our approximation remains valid while the matter freely falls to form the disk.

### 2.2.3 Initial formation of the disk

Just prior to infall, the shell is located at a large  $r$  value with  $u^a = (\gamma, 0, 0, \gamma\Omega)^a \partial_a$  such that  $u^t \gg u^r$  and therefore the shell falls from a near-rest configuration. For simplicity and compatibility with the MESA models, we assume that the stellar matter collapses in a shellular fashion with angular velocity  $\Omega = d\phi/dt$  (measured at  $r \rightarrow \infty$ ). The mass contained within such a shell at time  $t$  can be written as

$$dM = \int_{0,0}^{2\pi,\pi} T^{ab} u_a n_b dV, \quad (3)$$

where  $dV = \sqrt{g_{\Sigma_t}} dr d\theta d\phi$  and the integral is performed over  $\theta, \phi$  only. Here  $g_{\Sigma_t} = \det(g_{\mu\nu})$ ,  $g_{\mu\nu}$  being the induced metric on the spacelike hypersurface  $\Sigma_t$  at some time  $t$  calculated by setting  $dt = 0$  in the full Kerr metric  $g_{ab}$ . In addition,  $T^{ab} u_a$  ( $\approx -\rho u^t$ ) represents the energy-momentum density current and  $n_b = -dt/\sqrt{-g^{-1}(dt, dt)} = -dt/\sqrt{-g^{tt}}$  is the unit 1-form normal to  $\Sigma_t$ . Hence Eq. 3 yields

$$\begin{aligned} dM &= \int_{0,0}^{2\pi,\pi} \rho \frac{(a^2 \cos^2 \theta + r^2)^{\frac{3}{2}} \sin \theta}{\sqrt{a^2 \cos^2 \theta - 2mr + r^2}} dr d\theta d\phi \\ &\approx \int_{0,0}^{2\pi,\pi} \gamma \rho r^2 \sin \theta dr d\theta d\phi, \end{aligned} \quad (4)$$

where during the last approximation, we have dropped terms  $O(a/r)$  which is allowed if  $a \ll 1$  or  $r \gg M$ . We are interested in finding the stellar radius  $r_0$  at which the infalling shell has sufficient angular momentum to first form an accretion disk. This occurs when the (averaged) specific angular momentum  $\ell$  of the collapsed shell in the equatorial plane equals the specific angular momentum of the innermost stable circular orbit (ISCO)  $\ell_{\text{isco}}$  of the Kerr metric. At this point, the matter first circularises at the ISCO before plunging into the black hole. The angular momentum contained in the shell with mass  $dM$  can be written as

$$\begin{aligned} dJ &= \int_{0,0}^{2\pi,\pi} T^{ab} \eta_a n_b dV \\ &\approx \int_{0,0}^{2\pi,\pi} \gamma^2 \rho \Omega r^4 \sin^3 \theta dr d\theta d\phi, \end{aligned} \quad (5)$$

<sup>2</sup> Latin indices take the values 0,1,2,3 and Greek indices take the values 1,2,3.

where the approximation is again under the same condition as before. This implies that

$$\ell(r) = dJ/dM. \quad (6)$$

Additionally, the specific angular momentum at radius  $r$  of a circular orbit in the equatorial plane of the Kerr metric assuming prograde orbits is (Bardeen et al. 1972)

$$u_\phi(r) = \frac{M^{1/2} (r^2 - 2aM^{1/2}r^{1/2} + a^2)}{r^{3/4} (r^{3/2} - 3Mr^{1/2} + 2aM^{1/2})^{1/2}}. \quad (7)$$

Since the above is defined per unit rest mass, we set  $\gamma = 1$  in Eq. 4 and 5 to bring Eq. 6 to a similar form. Choosing  $r = r_{\text{isco}}$  in Eq. 7, the condition

$$\ell(r_0) = u_\phi(r_{\text{isco}}) \quad (8)$$

gives us the stellar radius  $r_0$  at which the infalling shell has sufficient angular momentum to first form an accretion disk.

The coordinate time interval  $\Delta t = t(r_0) - t(r_{\text{isco}})$  then gives us the disk formation time post core-collapse (within an error margin of a sound crossing time as the information of the collapse would take this much time to reach  $r_0$ ). As we discuss in Appendix A,  $\Delta t$  can be well approximated by the corresponding Newtonian free fall time. Hence, to simplify our calculations, here we use the latter approach for calculating  $\Delta t$ .

### 2.2.4 Evolution of the disk

Once Eq. 8 is satisfied, the subsequent infalling matter would first be assimilated into the disk before being accreted by the black hole or blown away in the wind. For the accretion phase, we restrict ourselves to the equatorial plane of the black hole, where the accretion disk will reside. The line element in the equatorial plane ( $\theta = \pi/2$ ) reads

$$ds^2 = - \left(1 - \frac{2M}{r}\right) dt^2 - \frac{4aM}{r} dt d\phi + \frac{r^2}{\Delta} dr^2 + \frac{A}{r^2} d\phi^2, \quad (9)$$

where  $A \equiv r^4 + r^2 a^2 + 2Mra^2$ . At a given time  $t$ , let the disk have rest mass  $M_d$  and angular momentum  $J_d$ . The effective disk radius  $r_d$  can be calculated by equating

$$u_\phi(r_d) = J_d/M_d, \quad (10)$$

where the term on the LHS is given in Eq. 7. The mass and angular momentum evolution of the disk can be written as

$$\dot{M}_d = \dot{M}_{\text{fb}} - \dot{M}_{\text{lost}}; \quad \dot{J}_d = \dot{J}_{\text{fb}} - \dot{J}_{\text{lost}}, \quad (11)$$

where the dot represents derivative w.r.t.  $t$ . Additionally, the mass and angular momentum assimilation rate into the disk ( $\dot{M}_{\text{fb}}, \dot{J}_{\text{fb}}$ ) due to fallback can be calculated using Eq. 4 and 5, while the mass and angular momentum dissipation rate from the disk ( $\dot{M}_{\text{lost}}, \dot{J}_{\text{lost}}$ ) will be calculated below.

The infalling matter in the disk is accreted on a viscous timescale. To account for the effect of wind outflow, we model the local accretion rate as a power law (Blandford & Begelman 1999)

$$\frac{dM_{\text{acc}}(r)}{d\tau} = \frac{M_d}{\tau_{\text{vis}}} \left(\frac{r}{r_d}\right)^s; \quad (r_t < r < r_d), \quad (12)$$

where  $s \in (0.3, 0.8)$  is a free parameter (Yuan & Narayan 2014) and we assume  $s = 0.5$ . We interpret Eq. 12 to model the accretion rate as measured from a locally nonrotating frame of reference ( $r, \theta = \text{const.}$ ). Such observers would have zero angular momentum (apart from the effect of frame dragging) and are also known as zero angular momentum observers (ZAMO). Here,  $\tau_{\text{vis}}$  is the local

viscous timescale (as measured by ZAMO) and is modeled using the [Shakura & Sunyaev \(1973\)](#)  $\alpha$  viscosity prescription as

$$\tau_{\text{vis}} \approx 2/(\alpha\Omega); \quad \Omega = \Omega_K - \omega, \quad (13a)$$

$$\Omega_K = \frac{u_\phi}{u^t} = \frac{M^{1/2}}{r_d^{3/2} + aM^{1/2}}; \quad \omega = -\frac{g_{t\phi}}{g_{\phi\phi}}. \quad (13b)$$

Here  $\Omega_K$ ,  $\omega$  is the angular velocity of the fluid element (in a circular orbit) and the angular velocity of the frame dragging, respectively, as measured by an observer at radial infinity. In addition,  $\Omega$  is the angular velocity of the fluid as measured by a ZAMO ([Bardeen et al. 1972](#)). It is expected that  $\alpha \in [0.01, 0.1]$  with theory supporting the lower value and observation the larger one ([King et al. 2007](#)). Here, we take  $\alpha = 0.01$ . A variation in the value of  $\alpha$  would influence the maximal value of  $a^* := a/M$  ([Sądowski et al. 2011](#)) and therefore may affect the evolution of the black hole (see Section 2.3.1). To transform Eq. 12 into the Boyer-Lindquist frame, we convert the ZAMO proper time to the coordinate time as

$$d\tau = \frac{dt}{\sqrt{-g^{tt}}}; \quad 1/\sqrt{-g^{tt}} = \sqrt{\Delta} \left( r^2 + a^2 + \frac{2a^2Mr}{\rho^2} \right)^{-1/2}. \quad (14)$$

In Eq. 12, for  $r \leq r_t$ , where  $r_t$  is some transitional radius, the disk undergoes efficient neutrino cooling, resulting in no wind mass loss and hence efficient accretion. We calculate  $r_t$  by setting the RHS of Eq. 12 to  $10^{-2.5}r_t/(2GM)M_\odot/\text{year}$  (e.g., [Kohri et al. 2005](#); [Chen & Beloborodov 2007](#); [Kumar et al. 2008](#)). When  $r > r_t$ , the disk enters the advection-dominated accretion flow regime (ADAF, [Narayan & Yi 1994](#); [Narayan & McClintock 2008](#)), where most of the disk mass is blown away in the winds. One can check that the net mass loss rate from the disk - owing to outflows and black hole accretion - yields

$$\dot{M}_{\text{lost}} = \frac{M_d}{\tau_{\text{vis}}\sqrt{-g^{tt}}}. \quad (15)$$

Additionally, the net angular momentum loss rate yields

$$\dot{J}_{\text{lost}} = \dot{J}_{\text{BH}} + \underbrace{\int_{r_t}^{r_d} u_\phi(r) d\dot{M}_{\text{acc}}(r)}_{\dot{J}_{\text{wind}}}, \quad (16)$$

where the former term is defined in Eq. 20 and the latter term,  $\dot{J}_{\text{wind}}$ , represents the angular momentum lost in the outflow, assuming that the wind removes the corresponding specific angular momentum from its location of origin. The integral can be evaluated as

$$\begin{aligned} \dot{J}_{\text{wind}} &= \frac{M_d}{\tau_{\text{vis}}} \frac{s}{r_d^s} \int_{r_t}^{r_d} \frac{u_\phi(r)}{\sqrt{-g^{tt}}} r^{s-1} dr \\ &\approx \frac{M_d}{\tau_{\text{vis}}} \frac{s}{r_d^s} \left[ \frac{2amr^{s-1}}{1-s} + \frac{2\sqrt{mr}^{s+\frac{1}{2}}}{2s+1} \right]_{r_t}^{r_d} \end{aligned} \quad (17)$$

To calculate the last term, we dropped terms  $\mathcal{O}(a/r^2)$  within the integral. This is more accurate than assuming a Schwarzschild geometry with the dropped terms becoming increasingly less unimportant as  $a$  decreases or  $r$  increases. For the case where  $a = 0$ , Eq. 17 reduces to the one given in [Kumar et al. \(2008\)](#). Finally, to incorporate the influence of the anti-parallel relativistic jets on the accretion flow, we assume that post disk formation, the polar region making an angle of  $\theta = 30^\circ$  with the rotational axis is promptly removed from the star.

### 2.3 Evolution of black hole with a Novikov-Thorne disk

In the early phase, while the disk is yet to form, we assume that the mass freely falls into the black hole without losing energy or angular momentum. After an initial disk formation, the subsequent disk

dynamics is modeled as discussed in Section 2.2.4. This is analogous to modeling the accretion flow as consisting of a relativistic, radiatively efficient, geometrically thin accretion disk that lacks the presence of large-scale magnetic field interactions with the black hole, also known as [Novikov & Thorne \(1973\)](#) disk (NTD).

For such an accretion flow, once the mass reaches  $r_{\text{isco}}$ , it is assumed to be directly accreted by the black hole, adding mass at a rate of

$$\dot{M}_{\text{BH}} = u_t(r_{\text{isco}})\dot{M}_{\text{acc}}(r_{\text{isco}}), \quad (18)$$

where

$$u_t(r) = \frac{r^{3/2} - 2Mr^{1/2} + aM^{1/2}}{r^{3/4} (r^{3/2} - 3Mr^{1/2} + 2aM^{1/2})^{1/2}}, \quad (19)$$

is the specific energy of a circular orbit at the radius  $r = r_{\text{isco}}$  ([Bardeen et al. 1972](#)). This also adds angular momentum to the black hole at a rate<sup>3</sup>

$$\dot{J}_{\text{BH}} = u_\phi(r_{\text{isco}})\dot{M}_{\text{acc}}(r_{\text{isco}}), \quad (20)$$

where, following [Bardeen et al. \(1972\)](#),  $r_{\text{isco}}$  is

$$\begin{aligned} r_{\text{isco}} &= M \left[ 3 + z_2 - \sqrt{(3-z_1)(3+z_1+2z_2)} \right], \\ z_1 &= 1 + (1 - a^2/M^2)^{1/3} ((1+a/M)^{1/3} + (1-a/M)^{1/3}), \\ z_2 &= \sqrt{3a^2/M^2 + z_1^2}. \end{aligned} \quad (21)$$

#### 2.3.1 Equilibrium spin of the black hole

In principle, as the black hole accretes mass (and hence angular momentum), its spin parameter will gradually approach the limit  $a = M$ . However, on considering the decelerating impact of disk-emitted photons on the black hole, [Thorne \(1974\)](#) found that the dimensionless spin parameter of the black hole  $a^* := a/M$  should converge to a value of  $a^* = 0.9978$ . Since both Eq. 6 and 19 are functions of  $a$ , hence, the equilibrium value of  $a^*$  becomes important<sup>4</sup>. More recently, [Sądowski et al. \(2011\)](#) recalculated this limit for the case of (advection dominated, optically and geometrical thick) slim accretion disks and found  $a^* = 0.9994$  for  $\alpha = 0.01$  and a  $10 \times$  super-Eddington mass accretion rate. Since these conditions also manifest in collapsar physics, therefore, in this work, we use the latter equilibrium value for  $a^*$  when modeling the accretion flow using an NTD.

### 2.4 Evolution of black hole with a magnetically arrested disk

Magnetic fields are considered to be crucial in extracting the rotational energy of the Kerr black hole to power the anti-parallel relativistic jets. Of particular interest are the predictions of general relativistic magnetohydrodynamic (GRMHD) simulations of a magnetically arrested disk (MAD) state (e.g., [Tchekhovskoy et al. 2011](#)). Here, the accretion disk is threaded by a strong vertical magnetic field that is dragged inward by the accretion flow resulting in an accumulation of magnetic flux near the black hole horizon. These magnetic fields can play a central role in extracting the rotational energy of the black hole ([Penrose & Floyd 1971](#); [Blandford & Znajek 1977](#)).

To calculate the effect of MAD on the black hole, in conjunction with Section 2.2.4, here we follow the approach of [Moderski &](#)

<sup>3</sup> Note that we have added the subscript ‘‘BH’’ to the variables to explicitly associate them to the black hole.

<sup>4</sup> E.g., for  $a^* = 0.9978, 0.9994, u_t(r_{\text{isco}}) \approx 0.68, 0.58$  respectively.

Sikora (1996), which accounts for the energy and angular momentum loss of the black hole due to the Blandford-Znajek mechanism as

$$\dot{J}_{\text{BH}} = \ell_{\text{in}} \dot{M}_{\text{acc,in}} - \frac{P_{\text{EM}}}{k \Omega_{\text{H}}}, \quad (22a)$$

$$\dot{M}_{\text{BH}} = u_{t,\text{in}} \dot{M}_{\text{acc,in}} - \frac{P_{\text{EM}}}{c^2}, \quad (22b)$$

where  $\Omega_{\text{H}} = r_{\text{H}}/(M_{\text{BH}}a)$  is the angular frequency of the black hole's event horizon (measured at  $r \rightarrow \infty$ ) and  $r_{\text{H}} = M + \sqrt{M^2 - a^2}$ . In the MAD state, the other variables above need to be determined from GRMHD simulations, for which we use the recent analytical fits provided in the 3D GRMHD study of Lowell et al. (2023) as

$$P_{\text{EM}} = \eta_{\text{EM}} \dot{M}_{\text{acc,in}} c^2; \quad \eta_{\text{EM}} = 1.063a^{*4} + 0.395a^{*2}, \quad (23a)$$

$$\ell_{\text{in}} = 0.86; \quad u_{t,\text{in}} = 0.97, \quad (23b)$$

$$k = \Omega_{\text{F}}/\Omega_{\text{H}} = \min(0.1 + 0.5a^*, 0.35). \quad (23c)$$

Here,  $P_{\text{EM}}$  is the electromagnetic flux leaving the black hole, which is primarily contained in the jets, Also,  $\Omega_{\text{F}}$  is the angular frequency of the magnetic field lines at the horizon. The subscript ‘‘in’’ represents the inner end of the accretion disk in the simulations of Lowell et al. (2023), which is not necessarily at the ISCO.

## 2.5 Electromagnetic energy of explosion

The energy radiated during a GRB may arise either due to the viscous dynamics of the accretion flow, e.g., via the Blandford & Payne (1982) mechanism (as is the case for an NTD) or a combination of the former plus the Blandford-Znajek mechanism, the latter robbing the black hole of its energy and angular momentum (e.g., for the case of a MAD). This energy would have to climb the gravitational potential well of the black hole in order to be observed by a distant observer.

### 2.5.1 Gravitational redshift of the emitted energy

We account for the energy lost due to the gravitational redshift of the radiation when measured by an observer at radial infinity as follows. For a stationary observer at radius  $r$ , its 4-velocity is  $u^a = \sqrt{-1/g_{tt}} \cdot \xi^a$ . The energy of a radially moving photon as measured by this observer at  $r$  is

$$E(r) = -g_{ab} p^a u^b = -\sqrt{-1/g_{tt}} g_{ab} p^a \xi^b, \quad (24)$$

where  $p^a$  is the 4-momentum of the photon. In addition,  $g_{ab} p^a \xi^b$  should remain conserved along the photon's geodesic, given  $\xi$  is Killing. As such, the observed energy at  $r \rightarrow \infty$  is given by  $E_{\infty} = -g_{ab} p^a \xi^b$ . Hence, the energy of radiation at infinity is related to its value at some radius  $r$  as

$$E_{\infty} = E(r) \sqrt{-g_{tt}}, \quad (25)$$

where  $g_{tt}$  is calculated at the radius  $r$  and  $E(r) = 1 - u_t(r)$  is the total specific energy emitted by the fluid element during its decent to radius  $r$  from infinity. For computational ease, we evaluate the  $g_{tt}$  term in Eq. 25 assuming  $r = 2r_{\text{acc}}$ , where  $r_{\text{acc}}$  is the radius at which the element is accreted (e.g.,  $r_{\text{acc}} = r_{\text{ISCO}}$  for an NTD). This is a fair approximation since roughly half of the energy would be emitted on each side of this value. On the other hand, if the energy is sourced from the spin of the black hole (e.g., in the MAD state), assuming that the photons move radially outward from the ergosphere (as we did in Eq. 25), the latter becomes a surface of infinite redshift. However, actual photons would contain angular momentum and hence be able to escape the ergosphere to infinity.

For our current purpose we somewhat ad hocly set  $r = 1.01 \times r_{\text{ergo}}$  if the energy is sourced from the spin of the black hole, where  $r_{\text{ergo}} = M + \sqrt{M^2 - a^2 \cos^2 \theta}$  is the outer radius of the ergosphere of the black hole, and we assume  $\theta = \pi/2$ .

### 2.5.2 Isotropic equivalent energy of explosion

We classify the collapsar explosion as a potential source of GRB if the isotropic equivalent energy  $E_{\text{iso}}$  that is received at the radial infinity is larger than  $10^{51}$  erg (Perley et al. 2016), i.e.

$$E_{\text{iso}} = \frac{\beta}{f} \int_{t_{\text{exp}}} E_{\infty} dt > 10^{51} \text{ erg}. \quad (26)$$

Above  $\beta = 0.01$  is the fraction of energy generated that is released in the form of radiation (with the rest lost in neutrinos). In addition, we set  $\beta = 1$  if the radiation energy is sourced from the spin of the black hole. The term  $f := d\Omega/4\pi$  represents the fractional probability that the jet aligns with the observer's line of sight, where  $d\Omega$  is the total solid angle spanned by the jet cones. Following the calibration of Bavera et al. (2022) we take  $f = 0.05$ .

## 3 RESULT

By numerically implementing the formalism discussed in Section 2, here, we assess the impact of the progenitor star's mass and angular momentum reservoir on the properties of the subsequently produced black hole, such as its mass and spin. For the latter, we provide fitting functions that can be readily used by future studies (in particular population synthesis) where the pre-collapse nature of the progenitor star is known.

### 3.1 Masses of black holes born from rotating progenitors

Fig. 1 and 2 show the masses of black holes born from the MESA evolved stellar models. For comparison, we use the Fryer Delayed remnant mass function as a source of reference. We find that there is a threshold explosion energy  $E_{\text{iso}}$  beyond which there is a sudden change in the masses of black holes as a function of the pre-explosion progenitor's mass  $M_{\text{exp}}$ . The magnitude of such an  $E_{\text{iso}}$  and the amount of depreciation in the resulting black hole mass is a function of the hydrodynamical nature of the accretion flow. In the case of the NT accretion disk, the resulting drop in the mass of black holes can be as large as 50%, see Fig. 2(a). The MA accretion flow in Fig. 2(b) tends to produce black holes with relatively larger masses as compared to the NT flow. However, these are still lower than those resulting from the convection-enhanced neutrino heating explosion, as showcased by the Fryer delayed mechanism.

We note that, unlike the case of NTD, for the MAD state, the threshold  $E_{\text{iso}}$  does not guarantee a downward shift in the black hole masses. For example, in Fig. 2(b), we find very luminous GRBs with  $E_{\text{iso}} \gtrsim 3 \times 10^{53}$  erg, that also produce relatively massive black holes. Such explosions result from progenitor stars that rotate sufficiently rapidly to experience a strong GRB, but not enough to experience a complete spin-down. To achieve the latter, a near maximally rotating black hole needs to accrete  $\approx 20\%$  of its initial mass (e.g., Jacquemin-Ide et al. 2023). However, the aforementioned luminous GRBs with larger black hole masses only develop an accretion disk during the later stage of their evolution, hence minimizing their chances of a complete spin-down.

For stars with relatively smaller reservoirs of angular momentum, the collapse is semi-direct, without much dependence on the nature of the accretion flow. For such stars, we find the masses of the black holes to be typically larger than those predicted by the Fryer delayed mechanism. Although for such slow rotators, one might expect convection-enhanced neutrino heating to additionally

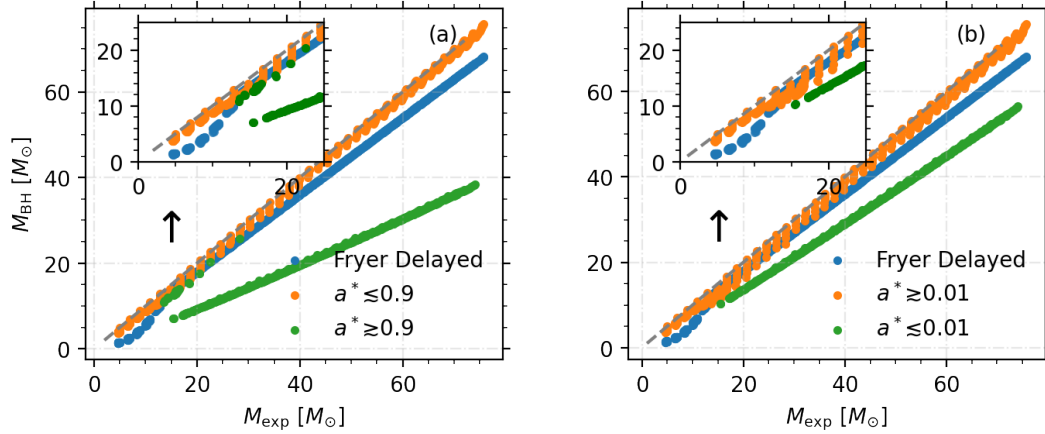


**Figure 1.** The masses of the black hole as a function of the final mass of their progenitor star (latter evolved till core carbon depletion). Figure (a) is for an NTD state, while Figure (b) is for the MAD state.

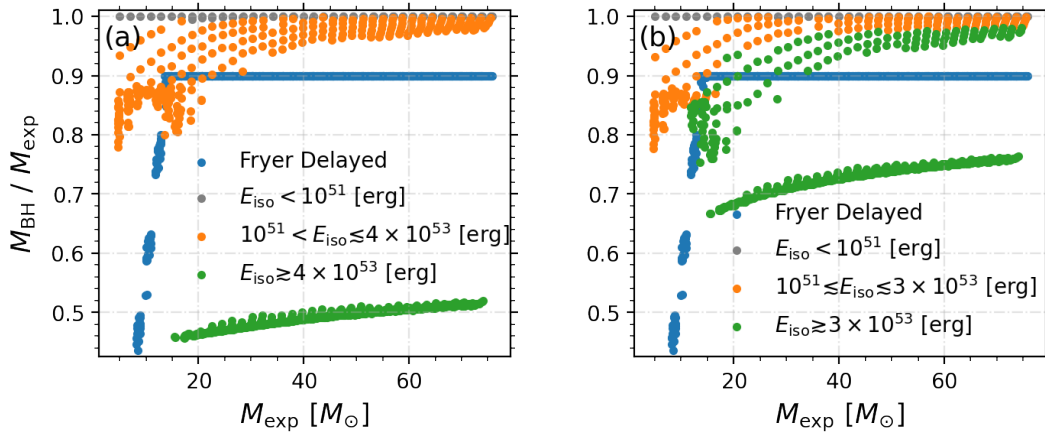


**Figure 2.** Same as Fig. 1 but now the y-axis shows the ratio of the black hole's mass to the pre-explosion mass of its progenitor star and the legend shows the isotropic-equivalent energy  $E_{\text{iso}}$  of the GRB.

contribute towards explosion energetics. However, the scarcity of observations of supernova explosions of stars with mass  $\geq 18 M_{\odot}$  suggests that direct collapse might be possible (Smartt 2015). Numerical studies (e.g., Murguía-Berthier et al. 2020) also align with observations, suggesting that massive stars might experience a direct collapse without an ensuing electromagnetic counterpart.

To better quantify the dependence of the black hole properties on the progenitor's structure, we now consider the full parameter space constituting the mass of the star prior to explosion  $M_{\text{exp}}$  and its (averaged) specific angular momentum reservoir  $\ell_{\text{exp}}$ . As shown in Fig. 3, in such a case, there appears to be a definite relation between  $M_{\text{exp}}$  and  $\ell_{\text{exp}}$  (i.e., the black dashed line):

$$\bar{\ell}_{\text{exp}} > (4 \times 10^3 M_{\text{exp}})^{1/2}; \quad \text{for } M_{\text{exp}} \geq 5 M_{\odot}, \quad (27)$$

where we first expect a GRB to take place and the black dotted line:

$$\bar{\ell}_{\text{exp}} > (7.5 \times 10^4 M_{\text{exp}})^{1/2}; \quad \text{for } M_{\text{exp}} \geq 15 M_{\odot}, \quad (28)$$

where we expect to see a strong deviation in the black hole masses  $M_{\text{BH}}$ . Here, for readability, we define  $\ell_{\text{exp}} := \bar{\ell}_{\text{exp}} \times 10^{14} [\text{gcm}^2 \text{s}^{-1}]$ . The corresponding fit function for the masses of the black holes can be approximated within 3% error (with 90% credibility; see Fig. B1)

as

$$M_{\text{BH}}^{\text{NT}} = \begin{cases} 0.38\sqrt{M_{\text{exp}}\bar{\ell}_{\text{exp}}} + 0.41\sqrt{M_{\text{exp}}} - 3.4\sqrt{\bar{\ell}_{\text{exp}}} \\ -0.72M_{\text{exp}} + 0.006\bar{\ell}_{\text{exp}} + 81; & \text{if Eq. 28 holds.} \\ 0.019\sqrt{M_{\text{exp}}\bar{\ell}_{\text{exp}}} - 0.065\sqrt{M_{\text{exp}}} - 0.051\sqrt{\bar{\ell}_{\text{exp}}} \\ +0.986M_{\text{exp}} - 0.0024\bar{\ell}_{\text{exp}} + 0.55; & \text{otherwise,} \end{cases} \quad (29a)$$

$$M_{\text{BH}}^{\text{MA}} = \begin{cases} -0.014\sqrt{M_{\text{exp}}\bar{\ell}_{\text{exp}}} - 0.076\sqrt{M_{\text{exp}}} - 0.077\sqrt{\bar{\ell}_{\text{exp}}} \\ +0.874M_{\text{exp}} + 0.0006\bar{\ell}_{\text{exp}} + 1.083; & \text{if Eq. 28 holds,} \\ 0.029\sqrt{M_{\text{exp}}\bar{\ell}_{\text{exp}}} - 0.424\sqrt{M_{\text{exp}}} - 0.055\sqrt{\bar{\ell}_{\text{exp}}} \\ +1.002M_{\text{exp}} - 0.0041\bar{\ell}_{\text{exp}} + 1.67; & \text{otherwise,} \end{cases} \quad (29b)$$

where the superscripts on  $M_{\text{BH}} [M_{\odot}]$  represent the assumption on the nature of the accretion flow during the collapse, and the constant coefficients have appropriate units to make the LHS and RHS dimensionally consistent. The parameter space lying above the boundary set by Eq. 28 is the region where the mass of the black hole experiences a sudden downward shift in trend. This shift can be attributed to the large reservoir of angular momentum of

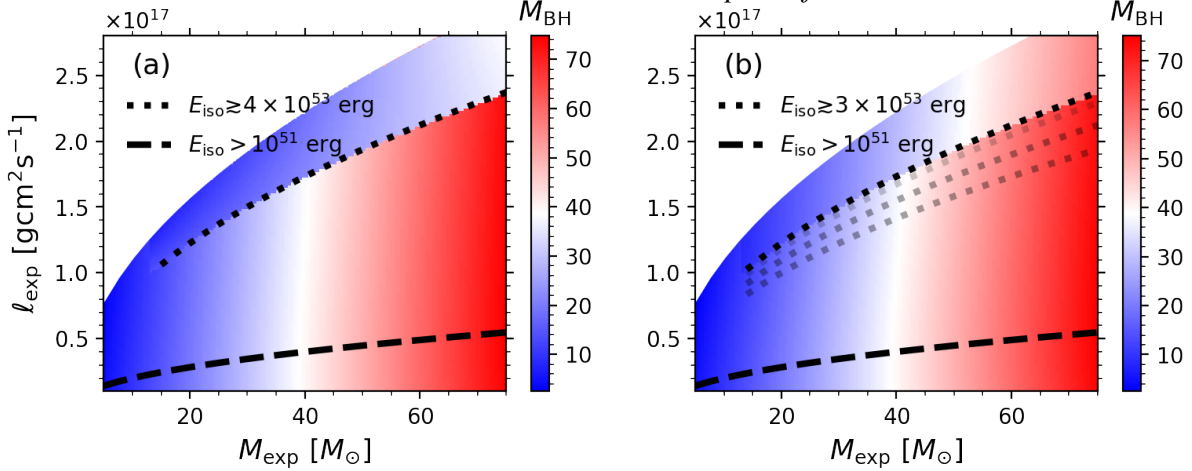


**Figure 3.** The masses of the black holes as a function of their progenitor star’s mass and angular momentum reservoir. The figures are drawn from the fits provided in Eq. 29. The x-axis represents the mass of the star and the y-axis is the specific angular momentum of the star at the point of core carbon depletion. Figure (a) is for the NT accretion flow, while Figure (b) is for the MA accretion flow. The region in gray dotted lines in Figure (b) corresponds to the very luminous systems in Fig. 2(b) that have  $E_{\text{iso}} \gtrsim 3 \times 10^{53}$  erg but do not satisfy Eq. 28 to experience a complete spin-down.

the progenitor, which causes the accretion disk to form promptly. After sufficient time, the accretion flow of such a collapse transforms into the ADAF regime (Blandford & Begelman 1999), resulting in a strong mass loss. Moreover, such NTD-hosting black holes also lose a considerable amount of mass in neutrinos from the inner region (owing to the URCA processes, Gamow & Schoenberg 1941), hence efficiently losing mass-energy to outgoing neutrinos. We note that the region plotted in gray dotted lines in Fig. 3(b) corresponds to the very luminous systems in Fig. 2(b) that have  $E_{\text{iso}} \gtrsim 3 \times 10^{53}$  erg but do not satisfy Eq. 28 to experience a complete spin-down or a substantial mass-loss.

### 3.2 Spin of black holes born from rotating progenitors

Similarly, Fig. 4 shows the dependence of black hole spin on the progenitors  $M_{\text{exp}}$  and  $\ell_{\text{exp}}$ . In the case of an NTD - see Fig. 4(a), for any given value of  $M_{\text{exp}}$  the black hole spin increases monotonically as a function of  $\ell_{\text{exp}}$ . Beyond a certain threshold value of  $\ell_{\text{exp}}$  (i.e., the dotted red line in Fig. 4, see Eq. 28), the black hole typically acquires a spin of  $a^* \gtrsim 0.9$ . This coincides with the region where the mass of the black hole experiences a sudden downward shift in trend in Fig. 3.

While in the case of an NTD, the GRB energetics fully result from the accretion dynamics, for a MAD, the spin angular momentum of the black hole plays a direct role in powering the jets. Consequently, we expect a dramatic variation in the final spin of the black holes depending on the nature of the accretion flow. This can be seen in Fig. 4(b), where the maximum attainable spin value is  $a^* \approx 0.65$ . This is because in the MAD state, the strongest GRBs - i.e., the systems lying above the dotted red line in Fig. 4(b) - rapidly spin down while also resulting in relatively lower mass black holes. However, as discussed previously, there is a region (plotted in dull-red lines) that results in strong GRBs but the  $a^*$  still remains large. The spin evolution of the black hole shown in Fig. 4 can be approximated within 12% error (with 90% credibility) as

$$a_{\text{NT}}^* = \begin{cases} -0.0021\sqrt{M_{\text{exp}}\bar{\ell}_{\text{exp}}} + 0.0024\sqrt{M_{\text{exp}}} + 0.052\sqrt{\bar{\ell}_{\text{exp}}} \\ +0.004M_{\text{exp}} - 0.0005\bar{\ell}_{\text{exp}} + 1.19 \times 10^{-6}M_{\text{exp}}\bar{\ell}_{\text{exp}} \\ -0.12; & \text{if Eq. 28 holds,} \\ -0.0016\sqrt{M_{\text{exp}}\bar{\ell}_{\text{exp}}} + 0.046\sqrt{M_{\text{exp}}} + 0.02\sqrt{\bar{\ell}_{\text{exp}}} \\ -0.0048M_{\text{exp}} + 0.0004\bar{\ell}_{\text{exp}} - 2.6 \times 10^{-6}M_{\text{exp}}\bar{\ell}_{\text{exp}} \\ -0.125; & \text{otherwise,} \end{cases}$$

$$a_{\text{MA}}^* = \begin{cases} 0.01; & \text{if Eq. 28 holds,} \\ -0.0006\sqrt{M_{\text{exp}}\bar{\ell}_{\text{exp}}} + 0.1162\sqrt{M_{\text{exp}}} + 0.0254\sqrt{\bar{\ell}_{\text{exp}}} \\ -0.0137M_{\text{exp}} - 0.0002\bar{\ell}_{\text{exp}} + 2.43 \times 10^{-6}M_{\text{exp}}\bar{\ell}_{\text{exp}} \\ -0.276; & \text{otherwise.} \end{cases} \quad (30a)$$

$$(30b)$$

The source of the larger error can be attributed to some data points that deviate from the general trend.

### 3.3 Domain of validity

Although it is challenging to measure the spin of individual components in a merging BBH, the mass-weighted effective spin parameter  $\chi_{\text{eff}}$  of the binary can be relatively well estimated from the observed gravitational wave signal. For a BBH comprising masses  $M_1$  and  $M_2$  with spins  $a_1^*$  and  $a_2^*$  aligned with their orbital angular momentum,

$$\chi_{\text{eff}} = \frac{M_1 a_1^* + M_2 a_2^*}{M_1 + M_2}. \quad (31)$$

Interestingly, recent findings suggest that most stellar mass black holes should be born with a negligible spin (Eggenberger et al. 2019; Fuller et al. 2019) with values around  $a^* \approx 0.01$  (Fuller & Ma 2019). Therefore, binaries with  $\chi_{\text{eff}} > 0$  might have a distinct formation history. The prevalent methods for generating spinning black holes in isolated binaries involve either (i) tidal spin-up of a progenitor star within a tight binary, with a fraction of the acquired angular momentum subsequently inherited by the ensuing black hole (e.g., Mandel & de Mink 2016; Marchant et al. 2016; Qin et al. 2018; Bavera et al. 2020), or (ii) sufficient mass (and hence angular momentum) accretion onto the progenitor star (e.g., Cantiello et al. 2007; Ghodla et al. 2023) or the first-born black hole (e.g., Zevin & Bavera 2022).

#### 3.3.1 Spin-up via tidal interaction

Tidal spin-up can occur while both stars are on their hydrogen main-sequence due to the occurrence of chemically homogeneous evolution (CHE e.g., Mandel & de Mink 2016; Marchant et al. 2016) or when the primary star first evolves into a black hole with

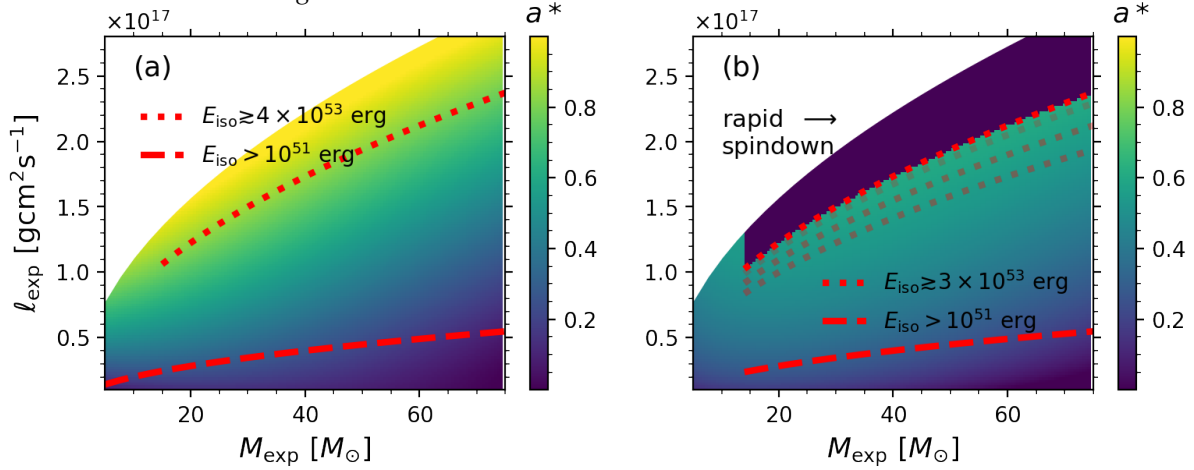


**Figure 4.** Same as Fig. 3 but now showing the dimensionless spin parameter  $a^*$  of black holes. Figures are drawn using the fits provided in Eq. 30.

now having a tidally locked secondary star that is on its helium main-sequence with negligible hydrogen envelope (e.g., Qin et al. 2018; Bavera et al. 2020; Fuller & Lu 2022). Assuming that the star’s spin period promptly synchronizes with its orbital period  $P$ , the value of such a star’s (averaged) specific angular momentum  $\ell$  can be estimated as

$$\ell = \frac{I\omega}{M_{\text{star}}} = \frac{2\pi r_g^2 R^2}{P}, \quad (32)$$

where  $I, \omega, M_{\text{star}}, r_g, R$  is the moment of inertia, orbital angular velocity, mass, radius, and radius of gyration of the star, respectively. Using Eq. 32 one can estimate the domain of validity of the fit functions provided in Eq. 29 and 30. For example, the blue curve in Fig. 5 shows the threshold minimum orbital period of the binary at the onset of helium main-sequence required to sufficiently spin-up the star - with  $Z \approx O(10^{-4})$  - for it to satisfy Eq. 28 by the time it reaches core carbon depletion. The orange curve, on the other hand, considers tidal synchronization till core helium depletion and therefore is applicable to high metallicity stars. This is because, post core helium depletion, the star with even larger metallicities will undergo relatively less mass loss and hence spin angular momentum loss.

### 3.3.2 Spin-up via mass accretion

Stellar spin-up via mass accretion might occur while the star is on its hydrogen main-sequence (Cantiello et al. 2007; Ghodla et al. 2023). For such systems, we expect the stars to undergo a GRB if they satisfy Eq. 27 at core carbon depletion. Additionally, the properties of the subsequently formed black hole could be highly affected if such systems also satisfy Eq. 28 (see Fig. 3 and 4). The latter is likely to be only valid in rapidly rotating low metallicity stars, i.e.,  $Z \lesssim O(5 \times 10^{-4})$  (Ghodla et al. 2023). However, in contrast to black holes born in tight binaries, we find that black holes born from stars that undergo accretion-induced spin-up do not merge efficiently unless the supernovae kick results in compact and/or significantly eccentric orbits. This is because to efficiently spin-up a star one likely requires the formation of an accretion disk around the mass gainer (e.g., Ghodla et al. 2023). However, for the formation of an accretion disk around the mass gainer, one needs to allow for a relatively larger separation between the binary components, which subsequently results in longer gravitational wave merger time. As such, although produced in relatively large numbers (e.g., Ghodla et al. 2023), such black holes might seldom feature in the BBH mergers detected on Earth by current-generation detectors.

## 4 DISCUSSION

In this work, we have adopted two types of accretion flows that could occur near the region surrounding the black hole during collapsar dynamics. While an MA accretion flow can be invoked to produce the anti-parallel GRB jets via the Blandford & Znajek (1977) mechanism, jets can also be produced in astrophysical objects lacking a black hole at the center (e.g., Metzger et al. 2011, 2017; Smith 2012). Hence, the energy of the jets need not come from the rotational energy of the black hole. For example, one can expect the formation of anti-parallel jets purely from the energy released during the accretion flow via the Blandford & Payne (1982) mechanism. Therefore, the approach of employing an NT accretion flow for the collapse dynamics is also relevant. However, a hydrodynamical flow (such as in the case of an NTD) would still require the presence of magnetic field lines to channel the outflow (Blandford & Payne 1982). In the following, we discuss some implications of the results detailed in Section 3 depending on whether an NTD or MAD operates to produce the GRB jets followed by some caveats and sources of uncertainty in our work.

### 4.1 Impact of stellar rotation on the lower end of PISN mass-gap

Stars with helium cores in the mass range of  $\approx 60M_{\odot} - 130M_{\odot}$  may develop the right condition for  $e^- e^+$  pair-production induced pair-instability supernova (PISN). This results in a (local) upper bound on the value of  $M_{\text{exp}}$  that could survive during core oxygen fusion (Fowler & Hoyle 1964; Rakavy & Shaviv 1967) without being completely disrupted due to the aforementioned process. Consequently, one also expects the formation of an upper mass-gap in the black hole mass spectrum.

However, rapid rotation can shift the lower boundary of PISN to larger  $M_{\text{exp}}$  values<sup>5</sup> (Glatzel et al. 1985). Marchant & Moriya (2020) found that for such systems, the lower edge of the black hole mass-gap can move upwards by 4% – 15% depending on the efficiency of angular momentum transport within the progenitor stars during their evolution. In contrast, the present work suggests that if the collapse of these rapid rotators<sup>6</sup> operates under the NTD formalism, such that the  $a^* \gtrsim 0.9$ , then the maximum black hole

<sup>5</sup> In this section we assume the largest  $M_{\text{exp}}$  that survives PISN is  $65M_{\odot}$ , cf. Farmer et al. (2019); Marchant & Moriya (2020)

<sup>6</sup> We allow for efficient angular momentum transport within the stellar interior aided by the Spruit (2002) dynamo. Turning this off would preserve more angular momentum within the star and result in favorable conditions for producing rapid rotators.



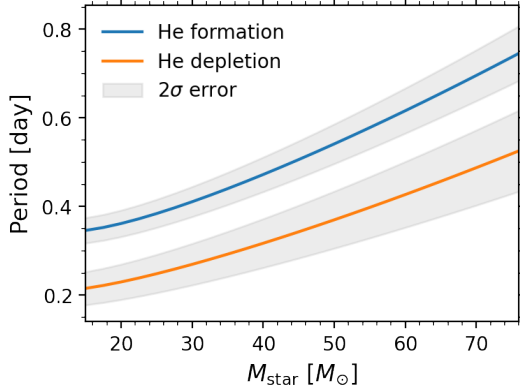


**Figure 5.** The maximum period at which the star would acquire and retain sufficient angular momentum to satisfy Eq. 28 by core carbon depletion. The blue and orange curves assume tidal locking at the onset of the helium main-sequence and core helium depletion, respectively. The x-axis shows the mass of the star at the onset of tidal locking, and the y-axis shows the period of the binary assuming that the other component is a black hole with mass ratio  $q = 1$ . The grey band of uncertainty results from the variance in the value of  $r_g$ .

mass should converge around  $M_{\text{BH}} \approx 35M_{\odot}$ . The latter value is much lower than the expected lower end of the mass-gap near  $M_{\text{BH}} \in \approx [45M_{\odot}, 55M_{\odot}]$ , e.g., Farmer et al. (2019); Marchant & Moriya (2020). Consequently, rapid rotators under an NT accretion flow seem unlikely to extend the lower end of the PISN mass-gap.

#### 4.2 Case for a massive and maximally spinning stellar black hole

We find that for MAD, the maximum black hole spin accumulates near  $a^* \approx 0.65$  while for an NTD it takes the value  $a^* \approx 1$ . However, for the latter, when  $a^* \approx 1$ , the collapsar energetic places an upper limit on the black hole mass as  $M_{\text{BH}} \lesssim 35M_{\odot}$ . Hence, irrespective of the nature of the accretion flow, the present work suggests that a near maximally rotating black hole (i.e.,  $a^* \approx 1$ ) with  $M_{\text{BH}} \gtrsim 35M_{\odot}$  might not result from stellar collapse. Instead, such a black hole could either be a second-generation black hole (i.e., a merger product of an earlier BBH system, e.g., Pretorius 2005; Fishbach et al. 2017; Gerosa & Berti 2017) or a product of subsequent mass (and angular momentum) accretion (e.g., Gammie et al. 2004; Sądowski et al. 2011). For the latter, super-Eddington accretion would be the likely scenario, as sub-Eddington accretion would make it difficult to spin up black holes to critical within the lifetime of a massive mass-donor star.

#### 4.3 A possible upper bound on $\chi_{\text{eff}}$ in black hole - helium star binaries

From Fig. 4, we see that for a given  $M_{\text{exp}}$ , a higher value of  $\ell_{\text{exp}}$  does not always lead to a larger  $a^*$ . Instead, once Eq. 28 is satisfied, the assumption of the nature of the accretion flow becomes crucial. For the case of MAD, a rapid spin-down is observed with  $a^* \approx 0$  (cf. Gottlieb et al. 2023; Jacquemin-Ide et al. 2023). This results in an upper bound on the spin with  $a^* \lesssim 0.65$ . In such a case, under the scenario that only the second-born black hole acquires spin in a tidally locked helium star-black hole binary, an upper bound on  $\chi_{\text{eff}}$  can be estimated as

$$\chi_{\text{eff,max}} = \frac{a_2^*}{q_{\text{max}}^{-1} + 1} \approx 0.325, \quad (33)$$

where  $q := M_2/M_1 \leq 1$  and we set  $q_{\text{max}} = 1$ .

On the other hand, the LIGO-Virgo-KAGRA collaboration

(Abbott et al. 2021b,a) has identified more than half a dozen candidate BBHs that do not respect this equality (see, e.g., Table B1). If MAD is the mechanism behind GRBs, this hints that an alternative scenario might be behind the formation of such BBHs. Tidal CHE can produce systems with large  $\chi_{\text{eff}}$  values since, in this case, both black holes can acquire large spin. However, the latter requires nearly equal mass-ratio binaries (Marchant et al. 2016), which is not the case for the black holes in Table B1. Alternatively, super-Eddington accretion onto the first formed black hole in an ordinary binary system can also generate a rapidly spinning (and massive) black hole. But the systems in Table B1 likely result from massive stellar progenitors that have a lifespan of only a few million years. This allows a tiny window for mass transfer, which implies the requirement of a rapid mass transfer rate supported by a very strong super-Eddington accretion. Additionally, the period of the binary should be such that they could subsequently merge within a few billion years. It is uncertain as to how likely these conditions could be met simultaneously.

A more plausible formation pathway for BBHs in Table B1 could be via hierarchical merger (e.g., Fishbach et al. 2017; Gerosa & Berti 2017; Kimball et al. 2021), e.g., in a triple system or dynamical capture in stellar clusters or in the disk of active galactic nuclei (AGN, e.g., Gerosa & Fishbach 2021; Arca Sedda et al. 2023 and reference therein). This is because the merger of even non-rotating black holes can result in second-generation black holes with  $a^* \approx 0.7$  (e.g., Pretorius 2005). Additionally, BBHs living in the disks of AGN also have the possibility of accreting mass and angular momentum from the disk.

#### 4.4 Comparison to the non-relativistic approach

A non-relativistic variant of the NTD formalism described in Section 2 is presented in Kumar et al. (2008) and later numerically implemented in Fuller & Lu (2022). We find the relativistic treatment to have a negligible effect on the final properties of the black hole. This is primarily because, during the initial stage of collapse, when near-horizon physics is important, most of the disk mass is efficiently accreted by the black hole due to the Urca processes (Gamow & Schoenberg 1941). Consequently, this hides the effect of a relativistic treatment in our time-averaged approach. During later stages, the disk circularizes at a relatively larger distance from the horizon, thus diminishing the effect of the Kerr geometry. However, the work presented in Section 2.5 is missing in the treatment of Kumar et al. (2008). Including this reduces the magnitude of  $E_{\text{iso}}$ , as measured by an observer at radial infinity by  $79 \pm 2\%$ ,  $85 \pm 5\%$  for an NTD and MAD state, respectively.

#### 4.5 Caveats and uncertainties

- The final structure of the star has been deemed crucial for the following explosion, with some massive stars producing a neutron star instead of a black hole, leading to the so-called islands of explodability (O'Connor & Ott 2011; Sukhbold et al. 2016; Sukhbold et al. 2018). Although it remains to be seen how this fares in the case of rapidly rotating stars where the dynamics of core collapse is dominated by the collapsar energetics. However, there is a possibility for a magnetar-like explosion (Woosley 2010; Kasen & Bildsten 2010) where the energetics are dictated by the magnetic fields of a proto-neutron star instead of a black hole. We ignore such a scenario in this work. As such, in our analysis, a black hole always forms during the collapse of the core of a massive star.

- At times, the stochasticity of the core structure can influence the nature of remnant masses. However, any stochasticity would be lost in our approach due to the averaging performed in the analysis. As discussed in Fryer et al. (2022), the effect of stochasticity would

nevertheless average out for a large enough sample size, which is always true in the context of population studies. This would also be the case with observations in the coming year as the number of gravitational wave detections grows.

- In the case of non/slowly rotating stars, our formalism results in a direct collapse. Although this might not necessarily be the case, the lack of detections of supernova explosions from high-mass stars (Smartt 2015) as well as the theoretical findings that more massive stars might disappear without leaving any observational feature (Murguía-Berthier et al. 2020), suggest that black holes forming from more massive stars might experience direct collapse. However, we note that stochastically varying angular momentum accretion on the proto-neutron star may form jittering jets (Papish & Soker 2011; Soker 2023), which could prevent direct collapse.

- For the case of an NTD, the accretion flow is circular and the disk truncates at the ISCO. However, numerical studies find that at a large accretion rate, the inner edge of the disk moves closer to the black hole but cannot be uniquely defined (Abramowicz et al. 2010). The flow also deviates from a Keplerian profile (Abramowicz et al. 2010; Sądowski et al. 2011), becoming super-Keplerian for our choice of  $\alpha = 0.01$ . We do not consider these aspects here. For rapid rotators, the ISCO will approach very close to the black hole, hence reducing our margin of error.

## 5 CONCLUSION

Black holes born from rapidly rotating progenitor stars can experience a very different supernova explosion than those born from non/slowly rotating stars. This is because a rapidly rotating star contains a large reservoir of angular momentum that it would need to lose to collapse below a certain characteristic radius. Here, we studied the resulting masses and spins of the black hole when dealing with the collapse of rotating stars. We showed that for rapid rotators, the black hole mass and spin is a function of assumption on the accretion flow and can be significantly different from that expected from a non/slowly rotating progenitor star (Section 3). This discrepancy could influence the merger time, luminosity distance, and gravitational wave properties of the BBH. We find that rapid rotators undergoing a collapsar explosion using an NT accretion flow might not extend the lower edge of the black hole upper mass-gap (Section 4.1) and that a maximally rotating black hole born directly from stellar collapse might have  $M_{\text{BH}} \approx 35M_{\odot}$  as its maximum possible mass (Section 4.2). For the case of an MA accretion flow, we find the maximum black hole dimensionless spin of  $a^* \approx 0.65$ . For black holes born in helium star black hole binaries, this puts an upper limit on the efficient spin of the BBH as  $\chi_{\text{eff}} \lesssim 0.325$  (Section 4.3).

## ACKNOWLEDGEMENTS

SG is supported by the University of Auckland doctoral scholarship. JJE acknowledges support of Marsden Fund Council managed through Royal Society Te Apārangi. This work utilized NeSI high performance computing facilities.

## DATA AVAILABILITY

The data underlying this article will be shared on reasonable request to the corresponding author. The numerical work discussed in Section 2 can be found at <https://github.com/SohanGhodla/Collapsar-Formalism>.

## REFERENCES

- Abbott The LIGO Scientific Collaboration the Virgo Collaboration the KAGRA Collaboration 2021a, arXiv e-prints, p. arXiv:2111.03606
- Abbott The LIGO Scientific Collaboration the Virgo Collaboration the KAGRA Collaboration 2021b, *Physical Review X*, **11**, 021053
- Abramowicz M. A., Jaroszyński M., Kato S., Lasota J. P., Różańska A., Sądowski A., 2010, *A&A*, **521**, A15
- Arca Sedda M., Naoz S., Kocsis B., 2023, *Universe*, **9**, 138
- Bardeen J. M., Press W. H., Teukolsky S. A., 1972, *Astrophysical Journal*, Vol. 178, pp. 347-370 (1972), 178, 347
- Batta A., Ramirez-Ruiz E., 2019, arXiv e-prints, p. arXiv:1904.04835
- Bavera S. S., et al., 2020, *A&A*, **635**, A97
- Bavera S. S., et al., 2022, *A&A*, **657**, L8
- Bekenstein J. D., 1972, *Phys. Rev. D*, **5**, 1239
- Bičák J., Stuchlík Z., 1976, *Monthly Notices of the Royal Astronomical Society*, **175**, 381
- Blandford R. D., Begelman M. C., 1999, *MNRAS*, **303**, L1
- Blandford R. D., Payne D. G., 1982, *MNRAS*, **199**, 883
- Blandford R. D., Znajek R. L., 1977, *MNRAS*, **179**, 433
- Blondin J. M., Mezzacappa A., DeMarino C., 2003, *The Astrophysical Journal*, **584**, 971
- Cantiello M., Yoon S. C., Langer N., Livio M., 2007, *A&A*, **465**, L29
- Carter B., 1971, *Phys. Rev. Lett.*, **26**, 331
- Chen W.-X., Beloborodov A. M., 2007, *ApJ*, **657**, 383
- Eddington A. S., 1925, *The Observatory*, **48**, 73
- Eggenberger P., den Hartogh J. W., Buldgen G., Meynet G., Salmon S. J. A. J., Deheuvels S., 2019, *A&A*, **631**, L6
- Eldridge J. J., Tout C. A., 2004, *MNRAS*, **353**, 87
- Farmer R., Renzo M., de Mink S. E., Marchant P., Justham S., 2019, *ApJ*, **887**, 53
- Fishbach M., Holz D. E., Farr B., 2017, *ApJ*, **840**, L24
- Fowler W. A., Hoyle F., 1964, *ApJS*, **9**, 201
- Fryer C. L., Kalogera V., 2001, *ApJ*, **554**, 548
- Fryer C. L., Belczynski K., Wiktorowicz G., Dominik M., Kalogera V., Holz D. E., 2012, *ApJ*, **749**, 91
- Fryer C. L., Karpov P., Livescu D., 2021, *Astronomy Reports*, **65**, 937
- Fryer C. L., Olejak A., Belczynski K., 2022, *ApJ*, **931**, 94
- Fujibayashi S., Shibata M., Wanajo S., Kiuchi K., Kyutoku K., Sekiguchi Y., 2020, *Phys. Rev. D*, **102**, 123014
- Fujibayashi S., Sekiguchi Y., Shibata M., Wanajo S., 2023, *ApJ*, **956**, 100
- Fuller J., Lu W., 2022, *MNRAS*, **511**, 3951
- Fuller J., Ma L., 2019, *ApJ*, **881**, L1
- Fuller J., Piro A. L., Jermyn A. S., 2019, *MNRAS*, **485**, 3661
- Gammie C. F., Shapiro S. L., McKinney J. C., 2004, *ApJ*, **602**, 312
- Gamow G., Schoenberg M., 1941, *Physical Review*, **59**, 539
- Gerosa D., Berti E., 2017, *Phys. Rev. D*, **95**, 124046
- Gerosa D., Fishbach M., 2021, *Nature Astronomy*, **5**, 749
- Ghodla S., Eldridge J. J., Stanway E. R., Stevance H. F., 2023, *MNRAS*, **518**, 860
- Glatzel W., Fricke K. J., El Eid M. F., 1985, *A&A*, **149**, 413
- Gottlieb O., Jacquemin-Ide J., Lowell B., Tchekhovskoy A., Ramirez-Ruiz E., 2023, arXiv e-prints, p. arXiv:2302.07271
- Herant M., Benz W., Hix W. R., Fryer C. L., Colgate S. A., 1994, *ApJ*, **435**, 339
- Israel W., 1967, *Phys. Rev.*, **164**, 1776
- Jacquemin-Ide J., Gottlieb O., Lowell B., Tchekhovskoy A., 2023, arXiv e-prints, p. arXiv:2302.07281
- Kasen D., Bildsten L., 2010, *ApJ*, **717**, 245
- Kimball C., et al., 2021, *ApJ*, **915**, L35
- King A. R., Pringle J. E., Livio M., 2007, *MNRAS*, **376**, 1740
- Kohri K., Narayan R., Piran T., 2005, *ApJ*, **629**, 341
- Kumar P., Narayan R., Johnson J. L., 2008, *MNRAS*, **388**, 1729
- Lee W. H., Ramirez-Ruiz E., 2006, *ApJ*, **641**, 961
- Lowell B., Jacquemin-Ide J., Tchekhovskoy A., Duncan A., 2023, arXiv e-prints, p. arXiv:2302.01351
- MacFadyen A. I., Woosley S. E., 1999, *ApJ*, **524**, 262
- Mandel I., de Mink S. E., 2016, *MNRAS*, **458**, 2634
- Marchant P., Moriya T. J., 2020, *A&A*, **640**, L18

Marchant P., Langer N., Podsiadlowski P., Tauris T. M., Moriya T. J., 2016, *A&A*, **588**, A50

Metzger B. D., Giannios D., Thompson T. A., Bucciantini N., Quataert E., 2011, *MNRAS*, **413**, 2031

Metzger B. D., Berger E., Margalit B., 2017, *ApJ*, **841**, 14

Meynet G., Maeder A., 1997, *A&A*, **321**, 465

Moderski R., Sikora M., 1996, *MNRAS*, **283**, 854

Murguía-Berthier A., Batta A., Janiuk A., Ramirez-Ruiz E., Mandel I., Noble S. C., Everson R. W., 2020, *ApJ*, **901**, L24

Narayan R., McClintock J. E., 2008, *New Astron. Rev.*, **51**, 733

Narayan R., Yi I., 1994, *ApJ*, **428**, L13

Novikov I. D., Thorne K. S., 1973, in *Black Holes (Les Astres Occlus)*. pp 343–450

O'Connor E., Ott C. D., 2011, *The Astrophysical Journal*, **730**, 70

Papish O., Soker N., 2011, *MNRAS*, **416**, 1697

Paxton B., Bildsten L., Dotter A., Herwig F., Lesaffre P., Timmes F., 2011, *ApJS*, **192**, 3

Paxton B., et al., 2013, *ApJS*, **208**, 4

Paxton B., et al., 2015, *ApJS*, **220**, 15

Paxton B., et al., 2018, *ApJS*, **234**, 34

Paxton B., et al., 2019, *ApJS*, **243**, 10

Penrose R., Floyd R. M., 1971, *Nature Physical Science*, **229**, 177

Perley D. A., et al., 2016, *ApJ*, **817**, 7

Pretorius F., 2005, *Phys. Rev. Lett.*, **95**, 121101

Qin Y., Fragos T., Meynet G., Andrews J., Sørensen M., Song H. F., 2018, *A&A*, **616**, A28

Rakavy G., Shaviv G., 1967, *ApJ*, **148**, 803

Riley J., Mandel I., Marchant P., Butler E., Nathaniel K., Neijssel C., Shortt S., Vigna-Gómez A., 2021, *MNRAS*, **505**, 663

Sądowski A., Narayan R., 2016, *Monthly Notices of the Royal Astronomical Society*, **456**, 3929

Shakura N. I., Sunyaev R. A., 1973, *A&A*, **24**, 337

Sharp D. H., 1984, *Physica D: Nonlinear Phenomena*, **12**, 3

Sądowski A., Narayan R., 2016, *MNRAS*, **456**, 3929

Sądowski A., Bursa M., Abramowicz M., Kluźniak W., Lasota J. P., Moderski R., Safarzadeh M., 2011, *A&A*, **532**, A41

Sądowski A., Narayan R., McKinney J. C., Tchekhovskoy A., 2014, *MNRAS*, **439**, 503

Smartt S. J., 2015, *Publ. Astron. Soc. Australia*, **32**, e016

Smith M. D., 2012, *Astrophysical Jets and Beams*

Soker N., 2023, *arXiv e-prints*, p. arXiv:2311.17732

Spruit H. C., 2002, *A&A*, **381**, 923

Sukhbold T., Ertl T., Woosley S. E., Brown J. M., Janka H. T., 2016, *ApJ*, **821**, 38

Sukhbold T., Woosley S., Heger A., 2018, *The Astrophysical Journal*, **860**, 93

Sweet P. A., 1950, *MNRAS*, **110**, 548

Tchekhovskoy A., Narayan R., McKinney J. C., 2010, *ApJ*, **711**, 50

Tchekhovskoy A., Narayan R., McKinney J. C., 2011, *MNRAS*, **418**, L79

Thorne K. S., 1974, *ApJ*, **191**, 507

Woosley S. E., 1993, *ApJ*, **405**, 273

Woosley S. E., 2010, *ApJ*, **719**, L204

Yuan F., Narayan R., 2014, *ARA&A*, **52**, 529

Zahn J. P., 1992, *A&A*, **265**, 115

Zevin M., Bavera S. S., 2022, *ApJ*, **933**, 86

du Buisson L., et al., 2020, *MNRAS*, **499**, 5941

## APPENDIX A: FREEFALL TIMESCALE

For a shell made of perfect fluid, the collapse is such that the coordinate  $\theta$  remains unchanged. This means that the trajectory of the particles would not cross each other during infall. Solving for the geodesic motion (assuming an infall from rest at radial infinity), one can show that for such a case

$$\frac{dr}{dt} = -\frac{(r^2 - 2Mr + a^2)[2Mr(r^2 + a^2)]^{1/2}}{(r^2 + a^2)^2 - (r^2 - 2Mr + a^2)a^2 \sin^2 \theta}. \quad (\text{A1})$$

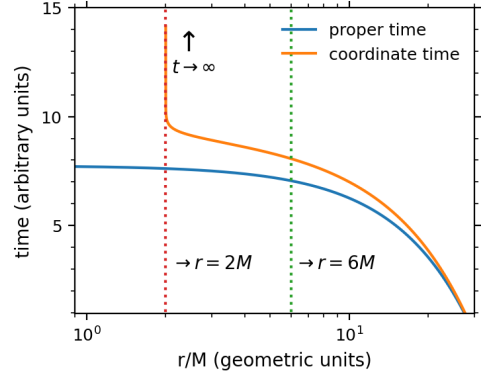


**Figure A1.** The deviation in the infall coordinate time and the infall proper time (in a Schwarzschild geometry), assuming that both time coordinates are synchronized at some fixed distance  $r_0 = 30M$ , which we approximate as the minimum distance from where an infalling shell would first circularize at ISCO ( $r = 6M$ ) in our work.

**Table B1.** LVK inferred parameters for systems with  $\chi_{\text{eff}} \geq 0.32$  (Abbott et al. 2021b,a)

Name	$M_1 [M_\odot]$	$M_2 [M_\odot]$	$\chi_{\text{eff}}$
GW190403_051519	$85.0^{+27.8}_{-33.0}$	$20.0^{+26.3}_{-8.4}$	$0.68^{+0.16}_{-0.43}$
GW190517_055101	$39.2^{+13.9}_{-9.2}$	$24.0^{+7.4}_{-7.9}$	$0.49^{+0.21}_{-0.28}$
GW200208_222617	$51^{+103}_{-30}$	$12.3^{+9.2}_{-5.5}$	$0.45^{+0.42}_{-0.46}$
GW170729	$50.2^{+16.2}_{-10.2}$	$34.0^{+9.1}_{-10.1}$	$0.37^{+0.21}_{-0.25}$
GW190805_211137	$46.2^{+15.4}_{-10.2}$	$30.6^{+11.8}_{-11.3}$	$0.37^{+0.29}_{-0.39}$
GW190620_030421	$58.0^{+11.2}_{-13.3}$	$35.0^{+11.3}_{-14.5}$	$0.34^{+0.22}_{-0.29}$
GW190519_153544	$65.1^{+10.8}_{-11}$	$40.8^{+11.5}_{-12.7}$	$0.33^{+0.20}_{-0.24}$
GW200306_093714	$28.3^{+17.1}_{-7.7}$	$14.8^{+6.5}_{-6.4}$	$0.32^{+0.28}_{-0.46}$

Eq. A1 depends on the coordinate  $\theta$ , implying that in a Kerr geometry, the equatorial part of a spherical shell falls faster than the polar region (e.g., Bičák & Stuchlík 1976). Integrating Eq. A1 when  $a \neq 0$  is difficult, and the resulting level of precision is not required here. For example, in Fig. A1, we compare the infall coordinate time (resulting from integrating Eq. A1 with  $a = 0$ ) with the infall proper time, assuming that both time coordinates are synchronized at some fixed distance  $r_0 = 30M$  (which we approximate as the minimum distance from where an infalling shell would first circularize at ISCO in our work). We find that upon reaching ISCO, there is  $\approx 12\%$  disagreement in the two time intervals. As  $r_0$  moves to larger values, this disagreement becomes smaller. E.g., for  $r_0 = 200M$ , it is reduced to  $\approx 2\%$ . Finally, when calculating the disk formation time  $\Delta t$  in Section 2.2.3, we note that the matter falls from a finite radius  $r_0$ , from a near-rest configuration, which also needs to be taken into account.

## APPENDIX B: ADDITIONAL MATERIAL

This paper has been typeset from a  $\text{\LaTeX}$  file prepared by the author.

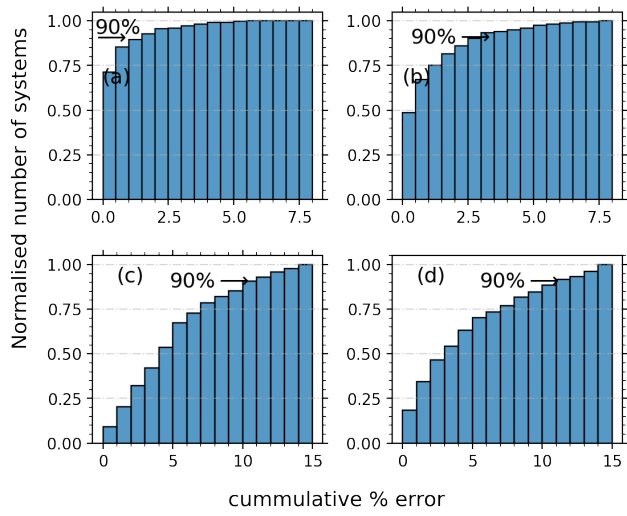


**Figure B1.** Figure (a) and (b) show the fitting error in the black hole masses given in Eq. 29, where Figure (a) is for NTD and Figure (b) for MAD state. Figure (c) and (d) show the fitting error in the black hole spins given in Eq. 30, where Figure (c) is for NTD and Figure (d) for MAD state.